Bulletin of the Seismological Society of America, Vol. 108, No. 6, pp. 3668–3683, December 2018, doi: 10.1785/0120170365

Ⓔ

Long-Term Monitoring of Induced Seismicity at the Insheim Geothermal Site, Germany

by L. Küperkoch, K. Olbert,* and T. Meier*

Abstract Induced seismicity associated with the geothermal power plant at Insheim (Germany) has been continuously analyzed using a combination of permanent and temporary stations since 2012 over a time span of more than 4 yrs. More than 600 induced events have been detected and located. The largest event had a magnitude of $M_L \approx 2.4$. Accurate locations are crucial for understanding the behavior of the reservoir. An initial velocity model derived from vertical seismic profiling (VSP) turned out not to be appropriate for the location of induced events. Location uncertainty was reduced by probabilistic earthquake locations using an optimized minimum 1D velocity model. Resolution was further increased by relative relocation based on differential travel times obtained from absolute *P*- and *S*-phase onset readings, as well as from waveform cross correlations. The initial absolute location errors decreased from 500 m horizontally and ≈1000 m vertically to ≈300 and ≈500 m, respectively. Clusters of similar events were detected by waveform cross correlation. The average difference in the relative locations between highly similar events amounts to about 50 m, yielding independent support for the relative location error estimate. Most of the events occur along a fault zone in the basement connecting the injection and the production wells. Interestingly, one cluster including the largest event occurred close to the production well. In addition, locations of induced events hint at the activation of formerly unknown conjugated fault zones. Derived fault-plane solutions of selected induced events confirm this interpretation and agree well with the regional stress regime. The seismically activated volume increased within 1 yr to its final volume of $\approx 1.65 \times 10^9$ m^3 and remained more or less constant. Seismic activity correlates strongly with injection rates and increases in case of unexpected shut-ins.

Electronic Supplement: Figures showing visualization of the 3D model derived from various 2D seismic campaigns, comparison between local magnitudes derived by the local earthquake survey (Landesamt für Geologie und Berbau Rheinland-Pfalz [LGBRP]) using calibrated stations and Wood–Anderson magnitudes derived by BESTEC GmbH using seismic stations of the Insheim network, magnitude scaling, applied quality assessment to derive onset time uncertainties, ray coverage of the Insheim reservoir, the results of the stability test of the inversion, and location uncertainties of a well locatable as well as of a less constraint induced seismic event.

Introduction

Deep geothermal energy (or deep-heat mining) has the potential to contribute significantly to the change from conventional energy supply to renewable energy (e.g., VanWees *et al.*, 2014). However, besides the high costs for drilling and the risk for nonsuccessful wells, induced seismicity accompanying deep geothermal projects turned out to be the key point for damping the boom of deep-heat mining projects, at least in central Europe. Because felt earthquakes were induced in Basel 2006 (Häring *et al.*, 2008), Landau 2009 (Bönnemann *et al.*, 2010), and St. Gallen 2013 (Diehl *et al.*, 2017), the acceptance for this energy source by the population has been challenged. Because of this, the main goal for geothermal power plant (GPP) operators is to avoid perceptible seismic events, whereas the flow rates have to be large enough for

*Also at Institute of Geosciences, University of Kiel, Otto-Hahn-Platz 1, 24118 Kiel, Germany.

an economic operation of the GPP. To avoid induced seismicity of larger magnitudes, it is necessary to understand the interdependencies between operation parameters (injection flow rate, injection pressure, injection temperature, injected volume, etc.) and the response of the reservoir. Crucial is the accurate location of induced seismic events.

Locating induced and thus shallow earthquakes still remains a challenging topic, especially in regions with complex subsurface structures. Furthermore, it is difficult to quantify the location uncertainty because source time and hypocenter, as well as an appropriate velocity model, are not known *a priori*. The uncertainty of earthquake locations is dominated by (1) measurement errors of seismic arrival times, (2) modeling errors of calculated travel times, and (3) the nonlinearity of the so-called "coupled problem of earthquake location and velocity model" (Kissling *et al.*, 1984; Husen and Hardebeck, 2010). According to Husen and Hardebeck (2010), measurement errors of arrival times that define the precision of the earthquake location described by the error ellipsoid of the earthquake location are referred to as the formal error; modeling errors of calculated travel times define the accuracy of the earthquake location and are mostly unknown. The accurate location of induced seismicity within the framework of deep-heat mining is of importance for the operator.

Within petrothermal systems, the induced seismicity is (1) a tool for creating heat-exchanger surfaces and (2) a tool for controlling the extent of the fluid paths within the primary dry rock matrix (e.g., Niitsuma *et al.*, 1999). Within hydrothermal systems, where natural fluids and fluid paths with sufficient permeability are available, the main aspect for accurate location is to control the extent of the seismically active volume and to distinguish between natural and induced seismicity (Dahm *et al.*, 2012). Both aspects are also of interest for petrothermal systems discussed here. Moreover, the location of a seismic event influences the determined magnitude and the calculated source mechanism that are, besides earthquake location, part of the so-called reservoir characterization. For reliable reservoir characterization, earthquake location uncertainties should be below a few tens of meters (Kinnaert *et al.*, 2016). However, Kinnaert *et al.* (2016) have shown that only a 5% uncertainty in the reference 1D velocity profile might lead to location uncertainties up to 650 m.

Here, using data obtained by long-term monitoring at the Insheim GPP, we discuss the earthquake location accuracy, the influence of velocity models, and propose a workflow for the location of induced events at geothermal reservoirs, including the relative relocation of a cluster of similar events. We further relate the locations and the source mechanisms to the fine-scale structure of the reservoir and discuss the spatiotemporal evolution of the induced seismicity.

The Geothermal Power Plant Insheim

The Insheim GPP is located in the central upper-Rhine graben (URG) close to Landau/Pfalz, Germany (Fig. 1), where the first hydrothermal power plant started operating in 2007. Energy production started in October 2012, and since then, besides a larger downtime at the beginning of 2013 due to a pumping failure and some minor downtimes due to revisions, the plant is continuously operating. Power generation of up to 4.8 MW is achieved by an Ormat-ORC (Organic-Rancine-Cycle) system with Isopenthan as working media. At the production well GtI2, fluid is pumped out by a liner-shaft pump with a 600 m liner (Fig. 2). After heat exchanging, the fluid pressure is still sufficient for reinjecting the fluids into the injection wells GtI1a/b (Fig. 2). The Insheim project is based on a multiformations reservoir concept (Baumgärtner and Lerch, 2013). The two wells GtI1a and GtI2 were drilled to 3.42 and 3.67 km depth in 2008 and 2009, respectively. Furthermore, to increase the injectivity index and to minimize the risk of larger induced seismic events, a sidetrack GtI1b was drilled in 2010 out of GtI1 from a 2.6 to 3.6 km depth. The open-hole sections of ~1000 m length are composed of fractured permo-triassic sediments and porphyritic basement. Fluid temperatures are above 160° C, with production flow rates between 60 and 70 l/s, whereas injection flow rates are ≈5 l/s less. Though planned production flow rates of 80 l/s have not been reached yet because of limited productivity of the production well, the power plant operates economically, due to a high amount of yearly production hours and a very good injectivity of the injection well that makes the use of an injection pump redundant and thus reduces the internal power consumption.

Because of favorable geological conditions, several deep-heat mining projects have been carried out in the URG. Besides the above-mentioned GPP Landau, which generates power up to 3 MW, the first operating hot dry rock (HDR)/enhanced geothermal system (EGS) power plant started at Soultz-sous-Forêts at the western boundary of the URG between Strassbourg and Karlsruhe in 1987 as a research project and generates up to 2.1 MW power (Fig. 1, Orywall *et al.*, 2009; Mergner *et al.*, 2012). Approximately 20 km to the north of Karlsruhe in Bruchsal, a hydrothermal power plant started operating in 2009, generating power up to 0.5 MW based on a Kalina process (Kölbel *et al.*, 2010; Mergner *et al.*, 2012). Close to Rittershoffen (northern Alsace, France, see Fig. 1), another geothermal project was initiated in 2011. This joint venture project is designed to deliver heat power of 25 MW through a 15 km transport loop from the drill site to the Rouquette Frères biorefinery in Beinheim (Baujard *et al.*, 2014).

Tectonic Settings

The URG is the part of the almost north–south trending, ~300-km-long European Cenozoic rift system in central Europe (Ziegler, 1992). Insheim is located close to the southern transfer zone that separates the northern URG from the southern URG (Derer *et al.*, 2005). The URG underwent three main subsidence episodes during the late Eocene to Early Oligocene, Latest Oligocene to Early Miocene, and

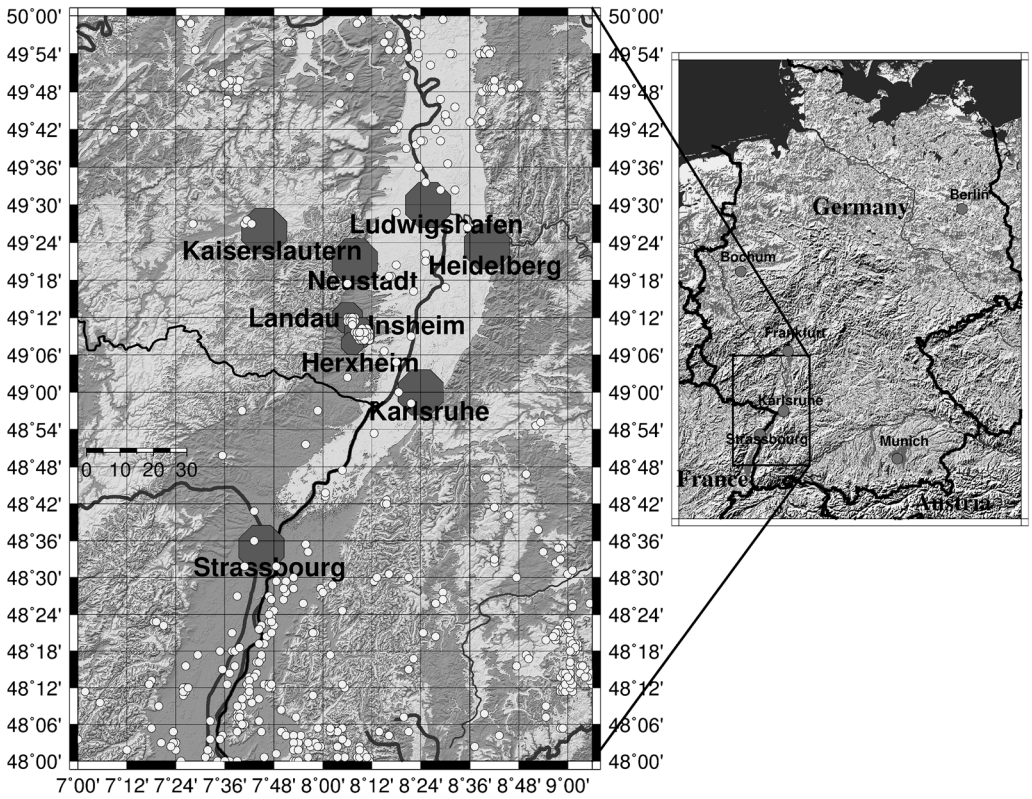

Figure 1. Upper-Rhine graben in southwest Germany. The geothermal power plant (GPP) Insheim is located close to Landau (~5 km airline distance). The background seismicity of the years 2012–2015 recorded by the regional earthquake survey is indicated by small circles. Induced seismicity at GPP Landau and GPP Insheim has partly been recorded by the regional earthquake survey.

Pliocene to Quaternary that partly exceeded, in total, 3.5 km that are mainly compensated by sediment filling (Derer *et al.*, 2005). Intense Cenozoic faulting and Tertiary extension resulted in complex subsurface, graben, and horst structures that are delimited by synthetic and antithetic faults, striking predominantly north–south to north-northeast–south-southwest (e.g., Schumacher, 2002). Four larger steeply dipping fault zones (yellow, green, blue, and red in Ⓔ Fig. S1, available in the electronic supplement to this article) have been identified by 2D seismic campaigns in the target area (Misiek *et al.*, 2009). The top of the granite basement in the vicinity of Landau and Insheim is located at depths between 2600 and 3400 m.

At depths of about 3000 m, the URG shows the strongest thermal anomaly in Germany, with temperatures above 160° C and distinct heat anomalies at Soultz-sous-Forêts (northern Alsace, France) and Landau (Pfalz, Germany) caused by ascending hot thermal water within a large groundwater convection cell. It is assumed that fluid transport responsible for hydrothermal heat redistribution in the sediments occurs mainly on rift and fault zones (Schellschmidt and Clauser, 1996; Pribnow and Schellschmidt, 2000).

The seismicity inside the rift and its boundaries is mostly moderate, with few events $M_L > 5$ in the last 1000 yrs (Leydecker, 2011). The strongest known earthquake occurred in 1356 in Basel, with an estimated macroseismic intensity of IX and an estimated seismic moment magnitude $M_w \approx 6.7–7.1$ (Fäh *et al.*, 2009; Leydecker, 2011). Recently, in the central URG an M_L 2.8 earthquake occurred at a lower crustal depth of about 22 km north of Speyer in February 2005, followed by two shallow thrust-faulting events with M_L 2.4 and 1.5 on the rift shoulder south of Heidelberg in March 2005 (Ritter *et al.*, 2005; Fig. 1). The most recent natural earthquake in the vicinity of the Insheim GPP that might have been felt by the population occurred in 21 August 2016 close to Herxheim, with a magnitude of M_L 1.2 (see Data and Resources).

Seismic Monitoring Network

A dense local seismic monitoring network has been deployed around Insheim, consisting of a high-gain network for monitoring microseismicity and a low-gain network for vibration measurements in buildings, in case of larger events. The low-gain network consists of 13 stations with 4.5 Hz three-component geophones and a Summit VIPA acquisition system (see Data and Resources). An event is detected by the low-gain network if a certain threshold (station specific between 0.01 mm/s ≤ thshld ≤ 0.1 mm/s) is exceeded. Thus, these stations provide waveforms only for larger events that might be felt by the population. The permanent high-gain network consists of nine permanent three-component stations (reduced to six permanent stations since March 2014) operated by the GPP (Pfalzwerke GmbH) and three perma-

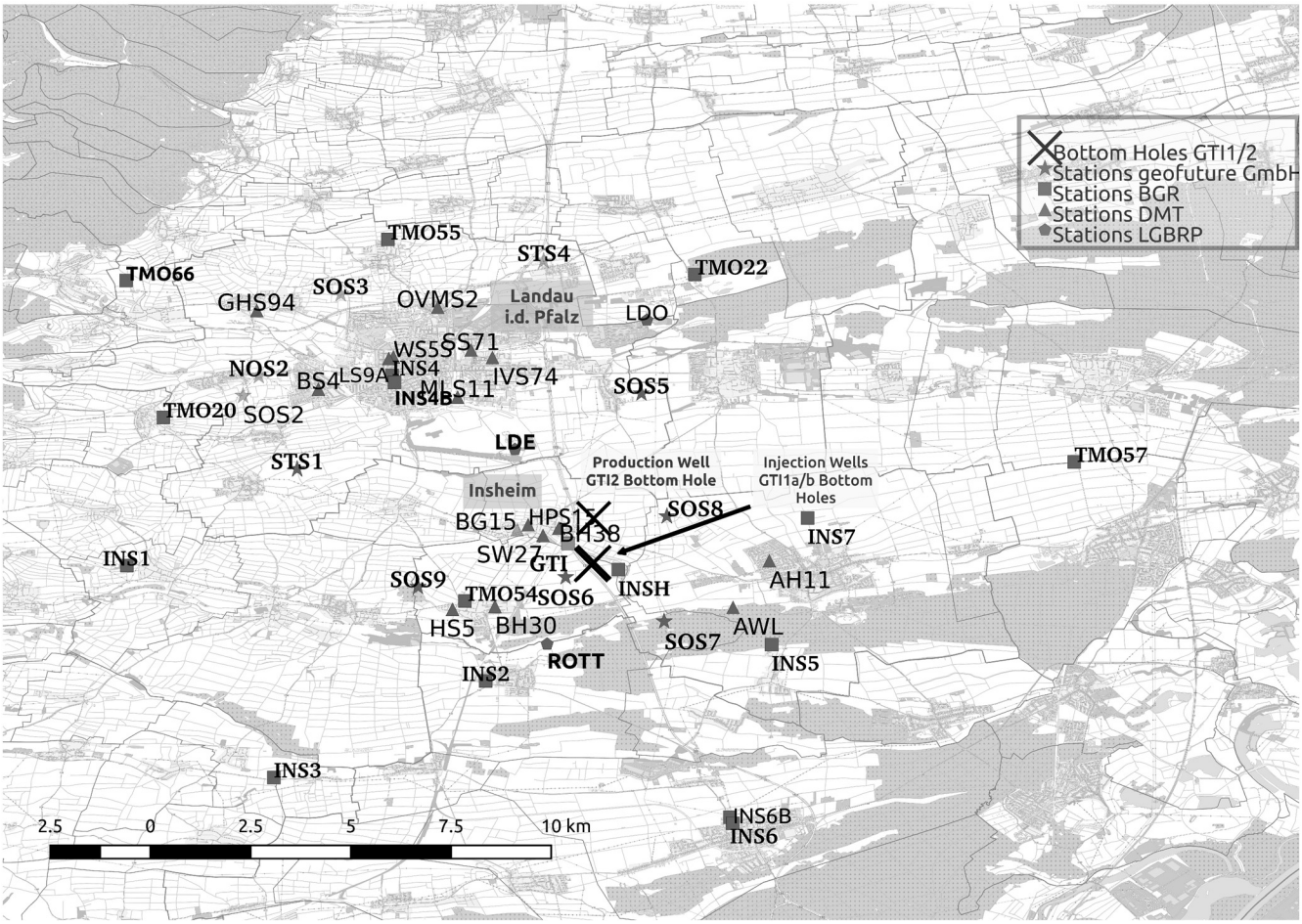

Figure 2. Seismic monitoring network consisting of initially 9 (reduced to 6 since March 2014) permanent and 30 temporary stations.

nent borehole stations operated by the regional earthquake survey (Landesamt für Geologie und Berbau Rheinland-Pfalz [LGBRP]). About 15 temporary stations were deployed at Insheim by the Federal Agency for Geosciences and Resources (Bundesanstalt für Geowissenschaften und Rohstoffe [BGR]) within the collaborative research project MAGS2 (Microseismic Activity of Geothermal Systems, Wegler *et al.*, 2017). The permanent stations operated by the GPP are equipped with Güralp 1 Hz Seismometers (CMG-6T) and Güralp acquisition systems. The three borehole stations are equipped with Lennartz-1Hz borehole seismometers (LE-3D/BH) at 76, 325, and 120 m depth, respectively. The data of these permanent stations are digitized at 100 Hz (200 Hz in case of the borehole stations) and transmitted via a mobile communication network to the data center at BESTEC GmbH, Landau. Events are automatically detected in near-real time by an enhanced short-term average/long-term average trigger and are automatically located using a collapsing grid-search algorithm (Applied Seismology Consultants, 2014). 400 Hz data are stored on-site on hard disks and are collected monthly for further offline data processing. The temporary stations of the BGR consist of Lennartz-3D Lite short-period sensors and Quanterra digitizers. One station is equipped with an STS-2.5 broadband seismometer. Data of the LGBRP and BGR stations are sampled at 200 Hz and are available in near-real time via SeedLink protocols or offline via ArcLink protocols. Figure 2 shows the seismological network, the GPP Insheim, and the landing points of the boreholes.

Induced Earthquakes at the Insheim Geothermal Reservoir

Nearly all deep geothermal reservoirs show induced seismicity, with fluid injection into crystalline rocks being more seismogenic than fluid injection into sedimentary rocks (e.g., Evans *et al.*, 2012). Though operating at low injection pressures (≈12 bars), the GPP Insheim generates seismicity, as is the case for other hydrothermal low-pressure GPPs (Megies and Wassermann, 2014). The temporal distribution of induced microseismicity at the Insheim reservoir clearly correlates, between October 2010 and December 2015, with the injection of fluids (Fig. 3). The GPP Insheim started operating on 13 October 2012. The first induced seismicity was observed on 20 October 2012. A first period of stronger seismic activity, with 84 detected induced events, occurred in November 2012. From December 2012 onward, the seismic-

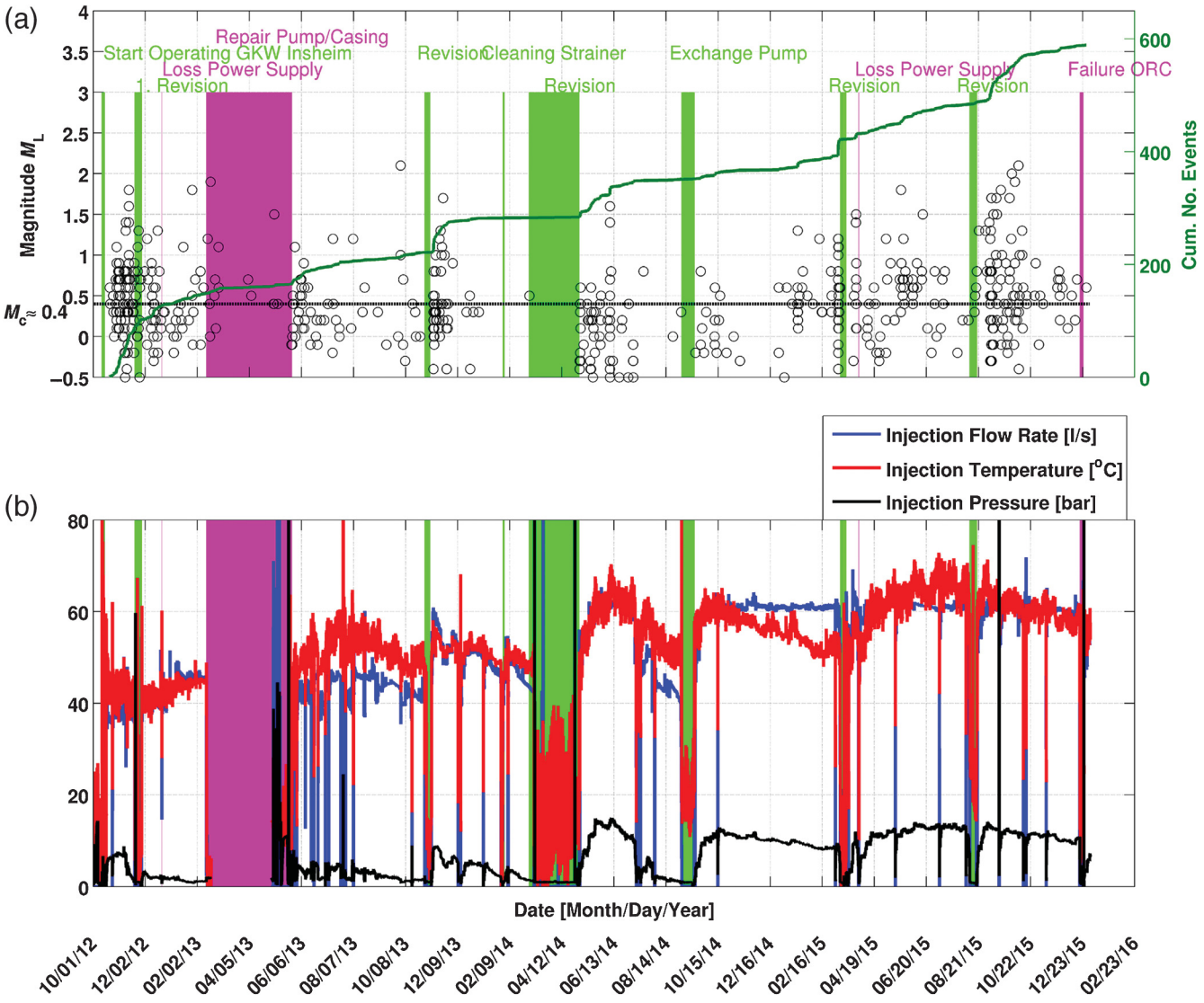

Figure 3. (a) Temporal distribution of seismic events and (b) corresponding operating parameters injection flow rate, injection temperature, and injection pressure. Shaded areas are planned (green) and unplanned (pink) downtimes of the GPP. The cumulative number of events is plotted on the right *y* axes. There is a clear correlation between seismicity rate and operation status; that is, downtimes and corresponding starting times of the GPP Insheim are followed by an increase of the seismicity rate.

ity rate declined. A power supply error forced the GPP Insheim to stop pumping immediately. A felt earthquake of $M_L \approx 1.9$ occurred 10 days after this sudden production stop. Remarkably, this event was also recorded by the pressure gauge in the well head of the production borehole. Therefore, this event should have occurred close to the production borehole. The location of this event is therefore roughly known, and we will refer to it later as a reference event.

After restarting the GPP Insheim almost three months later, the seismicity rate increased again but did not reach the level of November 2012. Figure 3 shows that that every startup of the GPP Insheim is accompanied by an increase in the seismicity rate that drops again after a few days. However, the operation at constant flow rate is also sometimes accompanied by induced seismicity that occurs predominately as earthquake swarms. Larger and possibly perceptible induced events are not exclusively correlated to downtimes or uptimes of the GPP Insheim.

Magnitudes have been calculated according to Stange (2006) as the empirically derived magnitude–distance correction terms are applicable to earthquakes in the study area with epicentral distances $10 \text{ km} \leq \Delta \leq 1000$ km. Magnitudes derived from recordings of the Insheim network show an offset compared to the corresponding magnitudes reported by the regional earthquake survey LGBRP. Thus, further scaling has been applied to remove the systematic offset of magntiudes (see Ⓔ Fig. S2). The resulting magnitude of completeness for the present earthquake catalog is $M_c \approx 0.4$. The largest induced events observed in the Insheim reservoir within the presented catalog estimated magnitudes between M_L 2.1 and 2.4. Compared to observed maximum magnitudes at other geothermal sites, the Insheim GPP falls into

the lower third of this ranking below Basel ($M_L^{max} = 3.4$) and Soultz-sous-Forêts ($M_L^{max} = 2.9$), also located in the URG (Zang *et al.*, 2014). The largest observed magnitude associated with geothermal exploitation has been observed in The Geysers, California, with a magnitude of $M_L = 4.6$ (Majer *et al.*, 2007; Evans *et al.*, 2012; Zang *et al.*, 2014). Groos *et al.* (2013) found that induced seismicity in the upper-middle Rhine graben might be perceptible down to magnitudes of $M_L \geq 1.2$. Based on this estimation, 54 induced seismic events listed in the current catalog might have been felt by the population. This very low perception threshold is caused by the shallow hypocentral depths and the unconsolidated sediments in the graben. The amplitudes measured at the surface are strongly site dependent, resulting in local variations in station magnitudes of up to $\Delta M_L \approx 0.7$.

Routine Earthquake Locations

For automatic online data processing, only six permanent stations (nine stations from October 2012 to March 2014) are available; for offline data processing, data of all available stations of the Insheim network, including low-gain and high-gain instruments, are used. All detections have been manually reviewed, and *P* and *S* phases have been picked manually. Quality measures have been assigned to all picks (see Ⓔ Fig. S3). HYPOSAT (Schweitzer, 2001) is used routinely for locating earthquakes using a nine-layer velocity model derived from offset-vertical seismic profiling (VSP) measurements carried out in 2009 (Misiek *et al.*, 2009). We refer to it as the VSP velocity model. For the VSP measurements, a three-component 15 Hz borehole sensor was deployed at 10 different depth levels in the injection well, whereas the sweep source (Vibrator AHV – IV) was deployed at 6 different positions. Sweep frequencies were varied from 20 to 70 Hz within 7 s (Misiek *et al.*, 2009). The sweep frequencies are similar to the dominant frequencies of induced microearthquakes at the Insheim reservoir that range from 10 to 50 Hz. The interpretation of the VSP measurements complemented by a borehole-derived stratigraphy and reinterpretation of a 2D seismic campaign in 1979 (Prakla Seismos GmbH) yielded a 3D subsurface model of Insheim and adjacent areas (see Ⓔ Fig. S1). The main reflectors are (1) top of granite (2824–3537 m depth), (2) top of Rotliegend (2431–3170 m depth), (3) top of red sandstone (2182–2917 m depth), and (4) top of Muschelkalk (2003–2668 m depth). Five main faults are identified, as well as a large number of subfaults (Misiek *et al.*, 2009). The main faults strike north-northwest–south-southeast and dip between 55° and 60° to the west. Two faults (green and blue in Ⓔ Fig. S1) are intersected by the boreholes GTI1/2. The derived 1D velocity model is shown in Figure 4, and the average V_P/V_S ratio was found to be 2.0. The very high V_P/V_S ratio is due to the very low *S*-wave velocities found in the vicinity of Landau and Insheim (Eulenfeld and Wegler, 2016) and accounts for the strongly unconsolidated sediments (very often pure sand) in the shallow layers. A high-velocity zone

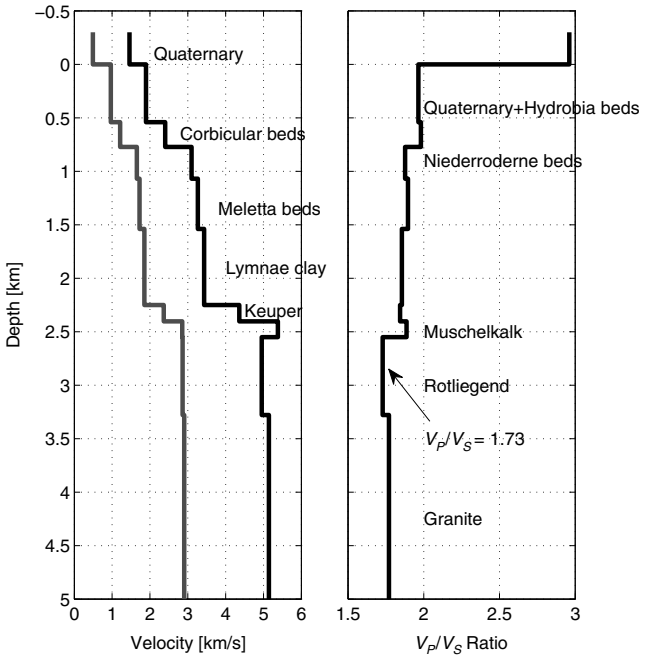

Figure 4. From VSP measurements derived velocity model (VSP velocity model) used for routine earthquake location in the Insheim reservoir.

(HVZ) with *P*-wave velocities larger than that for granite is found at a 2250 m depth that represents the Muschelkalk layer (Fig. 4). The *S*-wave velocities are less well resolved by active seismic exploration than the *P*-wave velocities; for example, the high-velocity Muschelkalk layer is missing in the VSP velocity model. Various studies showed the importance of accurate *S*-wave velocity models especially for hypocentral depth estimations (e.g., Gomberg *et al.*, 1990).

To improve locations with the VSP velocity model, station corrections have been calculated by comparing measured and theoretical arrival times of an assumed ground-truth event, for which an absolute source position has been assumed. This event correlated with the beginning of injection testing operations in the production well (Andrews and Pettitt, 2009). The resulting hypocenter locations of well-locatable events, for which at least eight picks are available and for which the maximum azimuthal gap is $\leq 180°$, are shown in Fig. 5a. From this figure, it becomes obvious that details of the spatial distribution of the induced events cannot be resolved using these locations. The low quality of the velocity model is also reflected by the relatively high root mean square (rms) travel-time residual of $rms_{TT} = 1.2$ s. Furthermore, the vast number of events are located between 7000 and 9000 m depth, which seems questionable because of fluid injection and production stretches between 2400 and 3600 m depth, respectively. Though the epicenter of the reference event is correctly found near the production well, its depth is much too large. The application of the VSP velocity model is thus inappropriate for accurate earthquake location at the Insheim reservoir because errors in the velocity model lead to unrealistic travel times, especially for the *S*

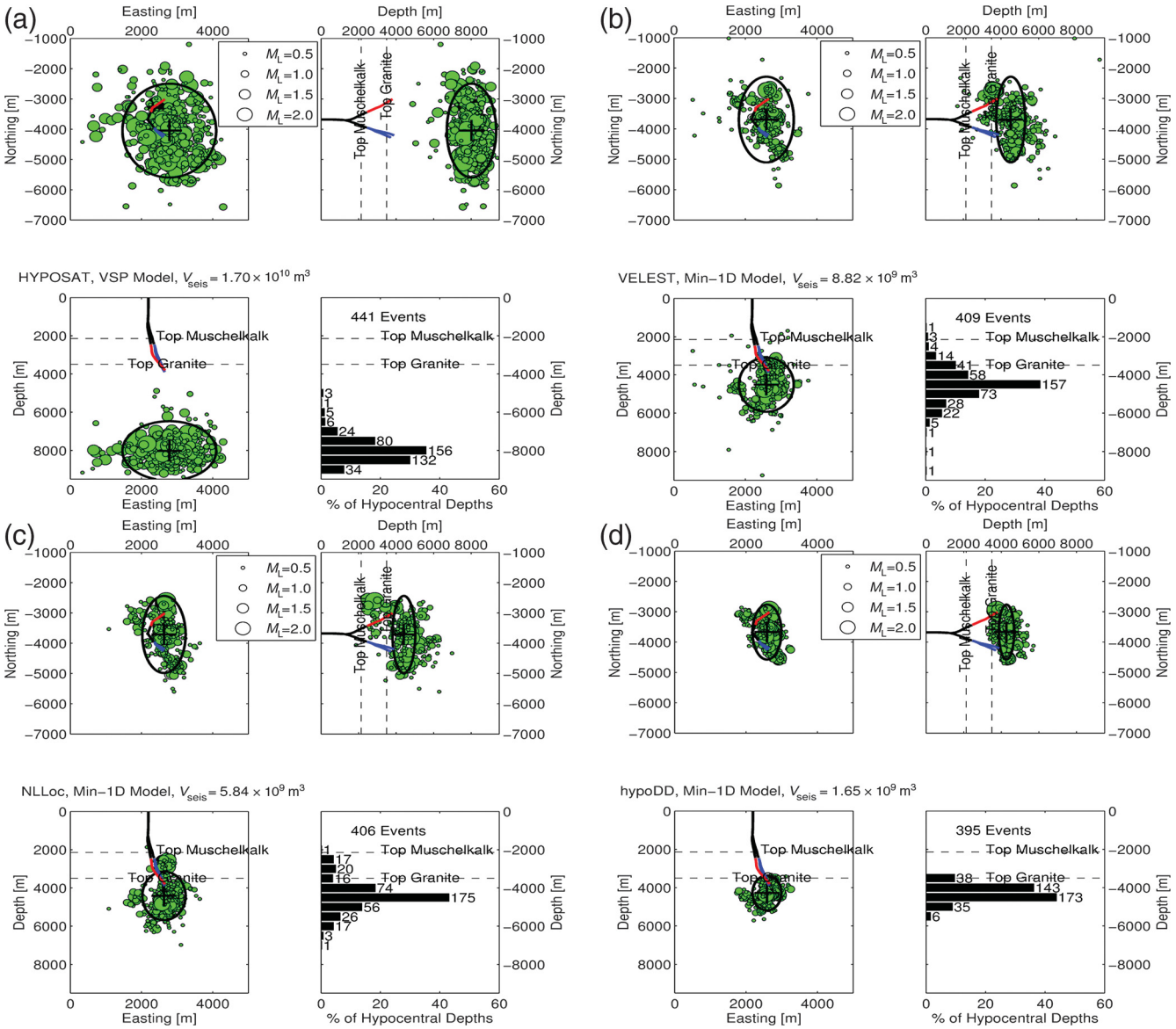

Figure 5. Epicenters calculated from (a) routine HYPOSAT earthquake location using VSP velocity model, from (b) VELEST inversion/location, from (c) NonLinLoc-probabilistic earthquake location, and from (d) hypoDD-double-difference earthquake location in plan view and cross sections along north-depth and east-depth profiles. Coordinates are relative to a reference point at borehole head GtLa1, GPP Landau. (b–d) are located using the new derived minimum 1D velocity model. Black ellipsoids indicate the estimated seismically active volumes. Black crosses show the calculated centroid. The distributions of focal depths indicate the uplift of determined focal depths and the shrinking of the seismically active volume with the various processing steps. Average depths of top of Muschelkalk and top of granite are indicated by dashed black lines.

waves. A new optimal velocity model and new station corrections for all available stations were calculated by joint inversion for hypocenters and *P*- and *S*-velocity models using the VELEST program (Kissling *et al.*, 1994).

Methods

Initial Velocity Models

All available *a priori* information were gathered and put into the initial starting models for the inversion using (1) the 2D seismic profiles from various campaigns in the vicinity of the borehole, (2) the offset-VSP measurements, (3) the stratigraphy derived from four boreholes, and (4) near-surface *S*-wave velocities from microzonation (Eulenfeld and Wegler, 2016). The derived borehole stratigraphies reflect the complex subsurface structure, because the granite basement is ∼1000 m deeper in Insheim than in Landau, though the boreholes are only ∼5 km apart from each other. Here, we combine this information to derive nine starting models for the inversion, using average values and their corresponding standard deviations of the layer depths. For each depth level, slow, fast, and average velocities are assumed (which yields $3 \times 3 = 9$ possible initial velocity models, Fig. 6). Following

Kissling *et al.* (1994), the only layers that have been integrated into the models are well resolved by controlled-source seismology and have been correlated to the borehole stratigraphy at the boreholes of the GPP Landau and the GPP Insheim. Layers with similar velocities have been gathered into one layer. No low-velocity zone (LVZ) was introduced into the initial *P*- and *S*-wave velocity models.

Calculation of a Minimum 1D Velocity Model

An optimal 1D velocity model was calculated using VELEST, a program to derive a so-called minimum 1D velocity model that represents the best approximation of the 3D subsurface structures by a 1D velocity model (e.g., Kissling, 1988). The derived station residuals account for velocity heterogeneity not taken into account by the 1D velocity model. VELEST solves the nonlinear, coupled hypocenter-velocity problem through a linearized iterative approach. Within each iteration step, arrival times for direct, refracted, and reflected waves are calculated, and the inverse problem (the determination of a velocity model and the source parameters) is solved by full inversion of the least-squares (LSQR) Jacobi matrix (Kissling *et al.*, 1994). For the inversion, 441 well locatable events with 6810 *P* picks and 6644 *S* picks of the routine locations were used (Ⓔ Fig. S3). However, important for a stable inversion is a dense ray coverage in the region of interest. Ⓔ Figure S4 shows the distribution of 441 selected events for the inversion procedure and the ray coverage in the Insheim reservoir, which has a sufficient density for the inversion purposes.

First, the inversion was done for each of the nine initial velocity models using only *P*-onset times, because the *P*-onset times are assigned with higher qualities than the *S*-onset times. As soon as the inversion procedure tried to implement an LVZ, several LVZs with velocities between 300 and 800 m/s slower than the above layer velocity were tested. However, because the Muschelkalk represents a HVZ, we also tried several HVZs with velocities between 400 and 800 m/s faster than the velocity of the layer below, instead of implementing an LVZ. Although the inversion with the LVZ yielded a minimum rms travel-time residual of $\mathrm{rms}_{\mathrm{TT}} \approx 0.07$ s, the inversion including a HVZ with a velocity 800 m/s faster than the layer below yielded a minimum rms travel-time residual of $\mathrm{rms}_{\mathrm{TT}} = 0.04$ s. This model was then used for a joint *P*- and *S*-wave inversion, with a constant V_P/V_S ratio of 1.9 for the initial *S*-velocity model (Fig. 7). The resulting model is less complex than the VSP velocity model, brecause only the most distinct layers with a sharp impedance contrast are taken into account, which can be assigned to (bio)stratigraphic beds.

To test the stability of the joint hypocenter inversion and to proof the complete sampling of the solution space, we randomly shifted the hypocenters from the locations obtained with the minimum 1D model. Then, we reintroduced them into the inversion to test the robustness of the new velocity model. Ⓔ Figure S5 shows that only a small systematic shift

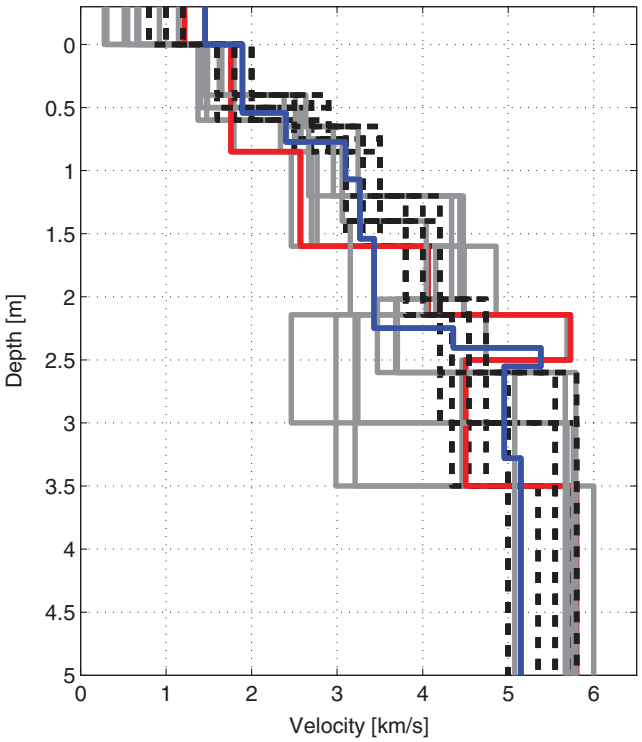

Figure 6. Initial (dashed) and final *P*-velocity models (straight, gray lines) after VELEST 1D inversion. For comparison, the VSP velocity model is shown (blue line). The optimum *P*-velocity model showing the lowest root mean square (rms) travel-time residual is shown in red. This model is further used for the joint *P*-/*S*-wave inversion. Initial velocity models did not include a low-velocity zone.

(on average about 450 m in the difference of the hypocenters) remains after the inversion between original and reshifted hypocenters, respectively. However, the stability test reveals that hypocentral depths are less constraint than epicentral locations.

Probabilistic Hypocenter Relocation

After determination of an optimal velocity model and corresponding optimized station corrections, the induced microearthquakes were relocated using the nonlinear probabilistic earthquake-location program NonLinLoc (Lomax *et al.*, 2000). This software is based on the probabilistic formulation of nonlinear inverse problems (Tarantola and Valette, 1982). It provides a direct analytic calculation of the maximum-likelihood source time by reducing the 4D problem (x, y, z, t) to a 3D problem (x, y, z). Furthermore, it determines a maximum-likelihood hypocenter, that is, a global minimum of the misfit function of the location-likelihood function using meshgrid algorithms. A 2D slowness grid was used with 2000 nodes in the east and north directions and 1000 nodes in the Z direction. The probabilistic density function for the spatial location and the origin time were computed with an oct-tree importance-sampling algorithm.

Ⓔ Figure S6 shows the resulting error ellipsoids, the Gaussian estimates of the locations, and, as an example,

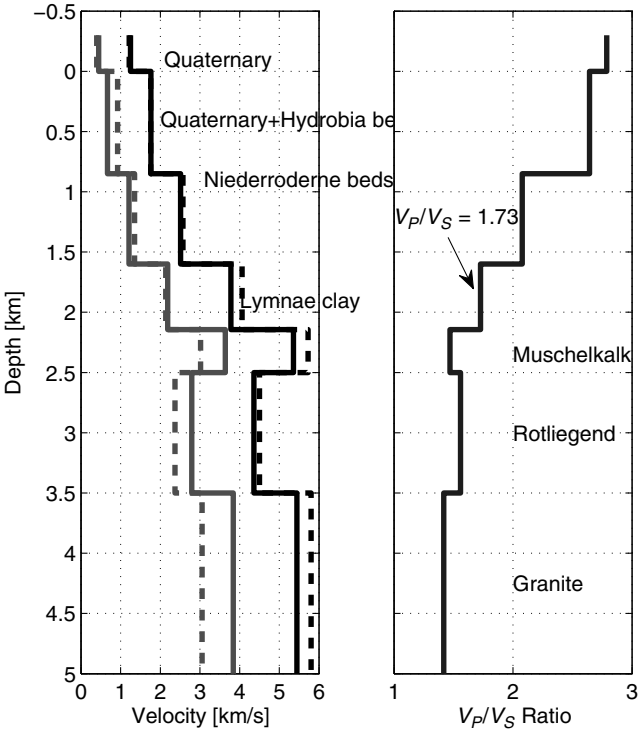

Figure 7. Initial (dashed lines) and final (continuous lines) *P*-/*S*-velocity model from joint VELEST inversion. The layers correlate with the observed stratigraphy.

the maximum-likelihood locations of two events with different numbers of onset times (green). For reasons of comparison, the error ellipsoids of the same events based on the VSP velocity model and old station corrections are also shown in blue. While the location of the event showing small error ellipsoids is based on 72 onset times ($M_L = 2.0$), the location of the event showing the large error ellipsoid is based on only 21 onset times ($M_L = 0.4$). Especially, the hypocentral depth of the latter event is much less constrained, showing an uncertainty of ~1 km, whereas the well-constrained event shows a hypocentral depth uncertainty of ~500 m. For both events, the error ellipsoids based on the VSP velocity model (blue) are much larger, indicating that the new velocity model is more reliable.

Double-Difference Hypocenter Relocation

In a last processing step, the determined maximum-likelihood hypocenters were improved by relative relocation, using the program hypoDD (Waldhauser and Ellsworth, 2000). Geiger's iterative location method for calculating absolute earthquake locations (Geiger, 1912) is extended in hypoDD, because this program minimizes the misfit between observed and calculated travel-time differences of event pairs, rather than the difference between observed and calculated travel times of single events. However, to apply this method, the following assumptions have to be fulfilled: (1) the hypocentral separation between two events must be small compared to the event—station distance and to the length scale of velocity heterogeneities, respectively, and (2) a homogeneous velocity structure within the source region is assumed. The adherence of these assumptions is justified for the induced seismicity recorded by the dense seismic network at Insheim. The use of double-difference travel times diminishes the influence of velocity heterogeneities, which avoids the need of station corrections. Relative travel times are calculated from neighboring events found with a nearest-neighbor approach from absolute travel times as well as from cross correlations of *P*- and *S*-wave phases. For the nearest-neighbor approach, a maximum distance of 15 km was adjusted (*MAXDIST* in hypoDD). The search radius was set to 0.5 km (*MAXSEP* in hypoDD), and a maximum number of 20 neighboring events was allowed (*MAXNGH* in hypoDD). Only neighbors that are linked with at least eight phase pairs (*MINLINK* in hypoDD) are considered to reach that number. For each event pair, a minimum of 8 observations (*MINOBS* in hypoDD) and a maximum of 30 observations (*MAXOBS* in hypoDD) were required. For details on these parameters, see Waldhauser (2001). The cross correlations are calculated for time windows of 0.6 s for *P* phases and 1 s for *S* phases, such that the full phase waveforms are included. Relative arrival times between events are considered if the waveform similarity exceeds cross-correlation coefficients (CC) of $CC \geq 0.8$. This threshold is large enough to ensure a high similarity of the events and low enough to obtain a large quantity of 185,000 relative travel times. The conjugate gradient method (LSQR, Paige and Saunders, 1982) was used to minimize the double-difference residuals for pairs of earthquakes at each station.

Results

Because of the presented workflow, the location uncertainty decreased significantly. The initial, provisional, and final results of hypocenter determinations using HYPOSAT, VELEST, NonLinLoc, and hypoDD are shown in Figure 5, respectively. After solving the coupled problem hypocenter determination–velocity model, the resulting minimum 1D velocity model is less complex and more similar for *P*- and *S*-wave velocities. The *P*-wave velocity of the Muschelkalk is now lower than that for granite, and the Muschelkalk is now also visible in the *S*-wave velocity model. The rms travel-time residual is reduced from $rms_{TT} = 1.2$ s to $rms_{TT} = 0.06$ s, which corresponds approximately to the average uncertainty of the *P* picks (see Ⓔ Fig. S3). Figure 8 shows the significant decrease of the individual *P*-wave and especially the *S*-wave station residuals. It is assumed that possible building responses are captured by the derived station corrections for stations located in buildings. The overall signs of station corrections remain the same for the VSP velocity model and the new minimum 1D velocity model. They hint at local heterogeneity, for example, in the western part of the study area.

The spatial distribution of the induced seismicity changed significantly from a more or less random distribu-

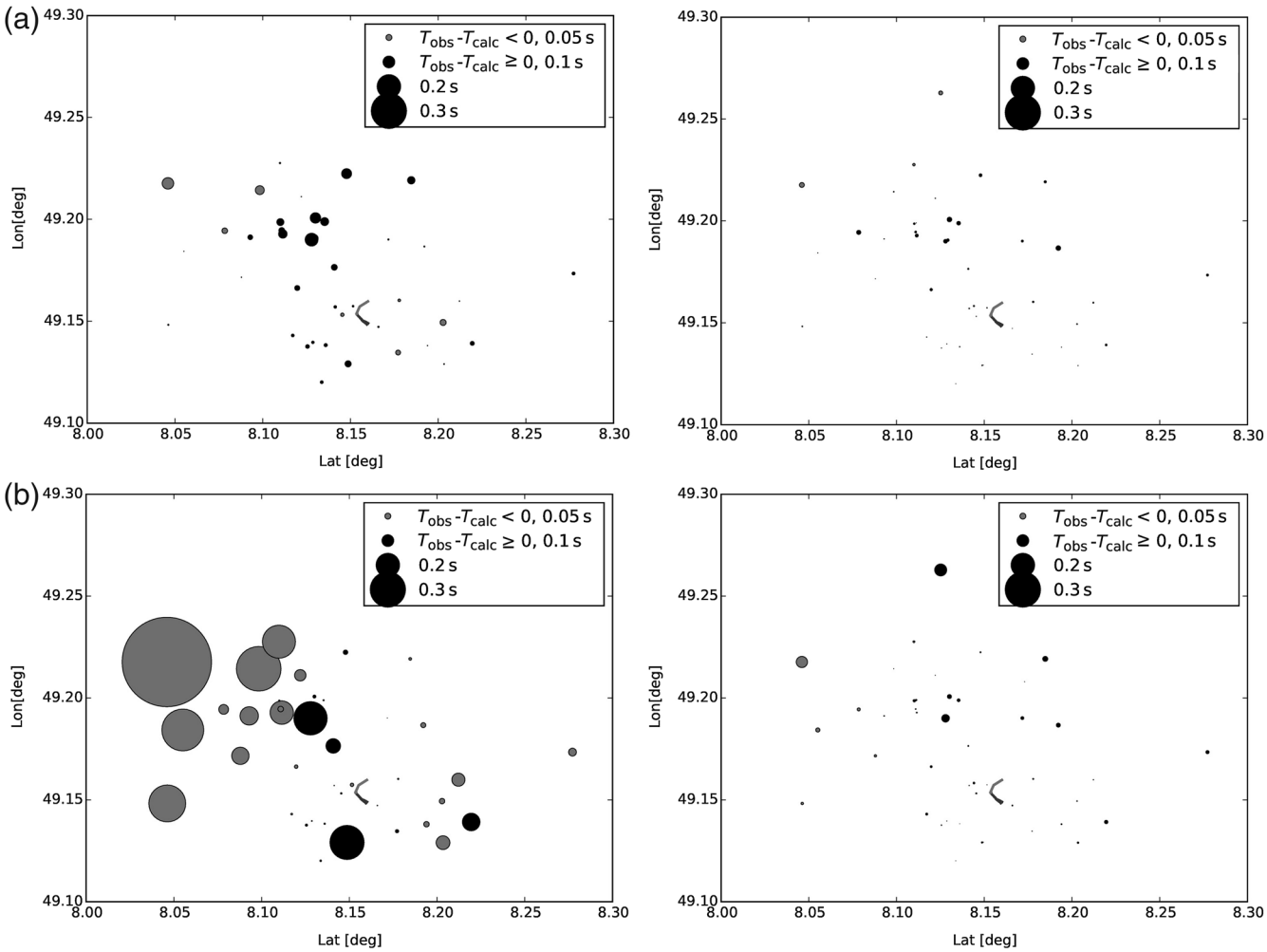

Figure 8. (a) Root mean square travel-time residuals of *P*-onset times and (b) rms travel-time residuals of *S*-onset times. To the left, station residuals found using the VSP velocity model; to the right. station residuals found using the new, minimum 1D velocity model. The size of the circles is proportional to the rms residual; black circles indicate positive rms residuals ($T_{obs} - T_{calc} > 0$, model faster than observation); gray circles indicate negative rms residuals ($T_{obs} - T_{calc} \leq 0$, model slower than observation).

tion to clustered hypocenters. The scatter in the hypocenter locations is reduced significantly and collapsed to four main clusters. Average hypocentral depths are lifted up from 8000–7000 m to 4000–2500 m (Fig. 5b). The reference event is lifted up from 7820 to 3700 m and is now located within a cluster close to the production well. Following Michelini and Bolt (1986), the seismically active volume has been estimated by calculating ellipsoids from the location-spread matrix, using principal component analysis. From that, the estimated, seismically active volume decreased from 1.7×10^{10} m^3 to 8.82×10^9 m^3 (compare Fig. 5a with 5b).

Subsequent application of NonLinLoc changed the picture of the observed induced seismicity further. The recalculated hypocenters are more strongly clustered, with less outliers (Fig. 5c). The cluster containing the reference event is shifted upward to a depth of ≈2600 m. The estimated active seismic volume decreased further to 5.48×10^9 m^3. Nearly all hypocenters are now located below the top of the Muschelkalk and not below ≈6500 m hypocentral depth.

The final double-difference relative location result is shown in Figure 5d. The location uncertainties are further reduced from $rms_{TT} = 0.06$ s to $rms_{TT} = 0.03$ s. Nearly the entire seismicity is now located in the granite, and only few events might have occurred in the above-consolidated Rotliegend sediments. The majority of earthquakes are located between 4000 and 4500 m depth. The reference event is now located realistically at about 3800 m depth in the very vicinity to the bottom of the production well. The entire seismically active volume decreased significantly to 1.65×10^9 m^3. The centroid (equal to the center of mass) is shifted to shallower depths from 7900 to 4200 m but changed only slightly in horizontal directions.

Waveform Similarity Analysis

A waveform similarity analysis has been performed to test the location accuracy and to detect clusters of similar events. Cross correlations between events are calculated

station-wise in a time window including both the *P* and *S* waveforms. As a result, 20 groups of similar events are identified, each with events showing CC ≥ 0.7 (see Table 1). About 340 out of 406 of the relocated events are assigned to event clusters, each marked by an individual color in Figure 9. Six main seismicity clusters are resolved: one cluster exactly at the production well including the largest observed events, one cluster to the west of the production well, one large cluster in the center of the reservoir, two clusters in the vicinity of the injection wells, and one small cluster to the east of the injection wells. However, the clusters of similar events between the injection and the production wells are spatially less distinct than the ones located at the production and injection wells, respectively (Fig. 9).

Events belonging to individual clusters are located in immediate vicinity to each other. Relocated hypocenters of events with similar waveforms having CC ≥ 0.7 show a median offset of 80 m. For higher similarities, CC ≥ 0.9, and the median hypocenter difference between events belonging to the same cluster decreases to less than 50 m. Assuming that the Green's function has a minor influence than the source function, this analysis additionally reveals the robustness of the location procedure and the significantly enhanced location resolution.

Table 1
Quantity of Seismic Events in 20 Differentiable Seismic Clusters at the Insheim Reservoir with Cross-Correlation Coefficients CC ≥ 0.7

Cluster Number	Number of Seismic Events
1	23
2	8
3	30
4	21
5	11
6	6
7	13
8	26
9	13
10	25
11	22
12	5
13	12
14	12
15	9
16	23
17	12
18	34
19	24
20	11

Discussion

The described optimization of the velocity model and the subsequent absolute and relative relocations of induced seismicity at the GPP Insheim revealed that the direct use of velocity models derived from active-source methods might be insufficient for reliable hypocenter determination. This has also been shown for induced seismicity at St. Gallen (Diehl *et al.*, 2017). Nevertheless, active-source methods are necessary for setting up initial velocity models and to analyze the subsurface structure in the vicinity of a GPP. In contrast, Maxwell and Young (1993) found a good agreement between controlled-source and passive-source velocity images. However, Maxwell and Young (1993) were able to use controlled seismic sources in the immediate vicinity of induced seismicity in a mine. At Insheim, source–receiver geometries used for VSP measurements differ considerably from source–station geometries of induced microearthquakes. This is likely the main reason for the VSP velocity model to be inappropriate for reliable hypocenter determination.

One limiting factor in this study might be the heterogeneity of the used data set, because the number of available *P*- and *S*-onset times varies between 8 and 36. The influence of station geometry and the number of available *S*-onset times has been shown in varies studies (e.g., Gomberg *et al.*, 1990; Husen and Hardebeck, 2010; Kinnaert *et al.*, 2016). Application of the presented method only on larger events with, for example, at least 30 available *P*-onset times is not possible, because then only too-few events remain for a joint hypocenter inversion. On the other hand, it might be necessary to include especially very weak events that might play an important role as precursors of larger and thus well locatable events, to which the weak events might be relatively located. However, the acquired data catalog with a magnitude of completeness of $M_c \approx 0.0$–0.4 limits the options of including such weak events. To reduce the magnitude of completeness in densely populated regions with strong anthropogenic noise, such as in Landau and adjacent regions, it would be necessary to replace at least partly the surface seismic network with a borehole seismic network.

The significantly improved location accuracy allows for detailed analysis of the spatiotemporal evolution of the induced seismicity, which is shown in Figure 9 with symbols and colors gathered by clusters of induced events and origin times grouped by quarters of years. During the early operation stage of the GPP, seismicity is induced in the vicinity of the injection well and to the west of the production well. The spatiotemporal evolution of the early seismicity indicates a migration of seismic events from the injection borehole toward the north-northwest along a known fault in the direction of the production well. In addition, the cluster of induced events indicate the activation of a former unknown northwest–southeast-trending fault zone. This may indicate a conjugated fault system to the known north–south faults that is active only in the first months of the production. Seismicity along this conjugated fault zone ceases after several months of production, and induced events occur only along the known north–south-directed fault zone (see Ⓔ Fig. S1). This orientation coincides with other known fault systems in the central upper-Rhine graben (Peters and van Balen, 2007).

For selected induced microearthquakes with local magnitudes $M_L \geq 1.1$, fault-plane solutions (FPS) have been calculated from first-motion polarities using the program HASH

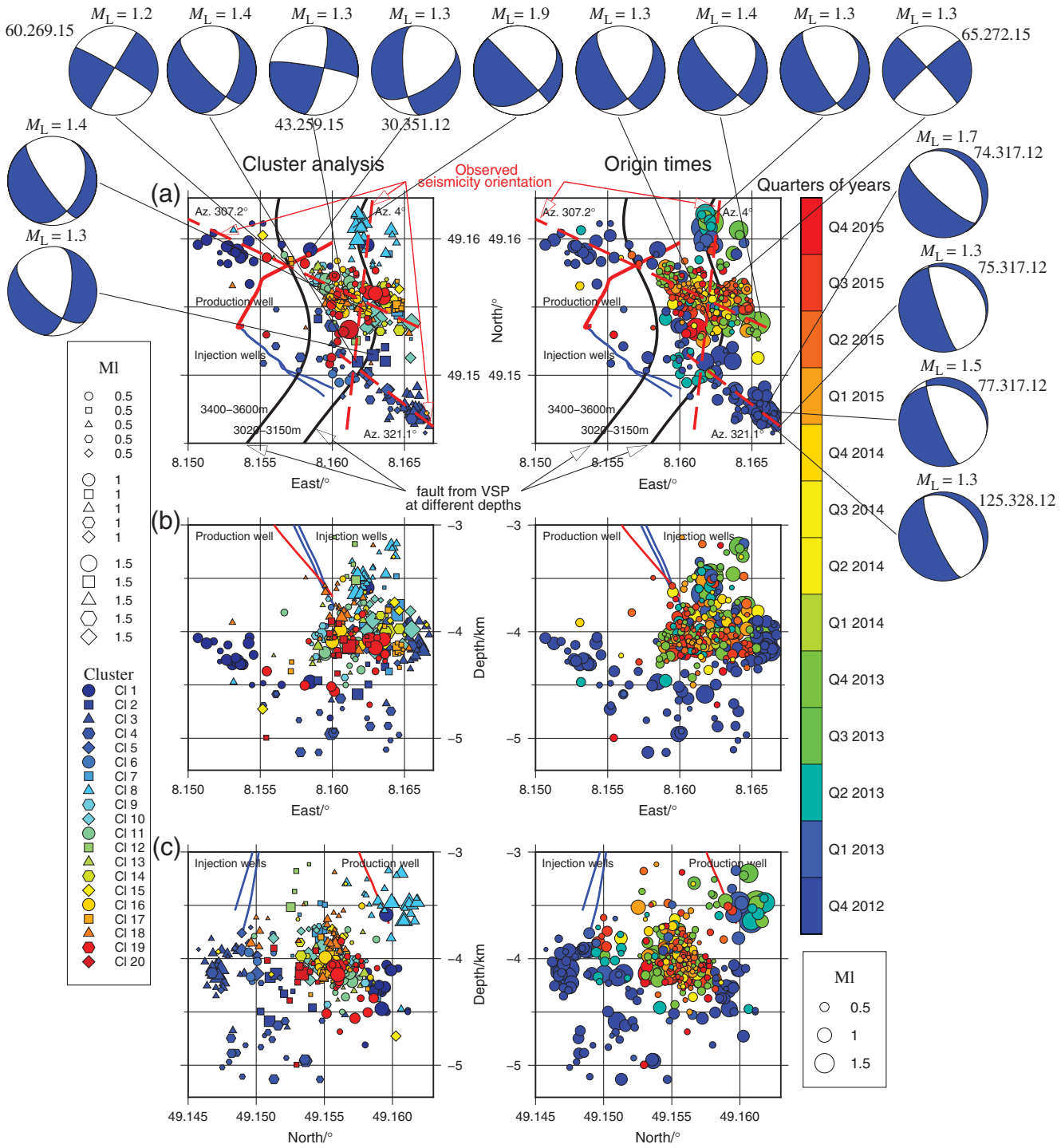

Figure 9. HypoDD-double-difference earthquake locations and fault-plane solutions of selected events in (a) plan view, (b) east–west profile, and (c) south–north profile. (Left column) Groups of symbols and colors indicate groups of clusters of induced events with combined *P*- and *S*-wave similarities CC ≥ 0.7. (Right column) Colors indicate origin times grouped by quarters of years. Black lines represent fault orientations known from VSP measurements. Red, straight, and dashed lines indicate likely conjugated fault orientations.

(Hardebeck and Shearer, 2002). Only robust, quality-A FPS (average misfit ≤ 0.15, rms fault-plane uncertainty ≤ 25°, station distribution ratio ≥ 0.5, mechanism probability ≤ 0.8, see the HASH manual for details) have been taken into account. Robust FPS are available for at least one event of cluster 1, 2, 3, 7, 8, 10, 18, and 20, respectively (Fig. 9). The majority of derived FPS shows north-northwest–south-southeast-striking, oblique normal faulting, and correlates well with the strike of the main known fault and the direction of S_H, which varies between north–south and north-northwest–south-southeast in the URG (Reiter *et al.*, 2015). However, a considerable variability is also present in the FPS: one event

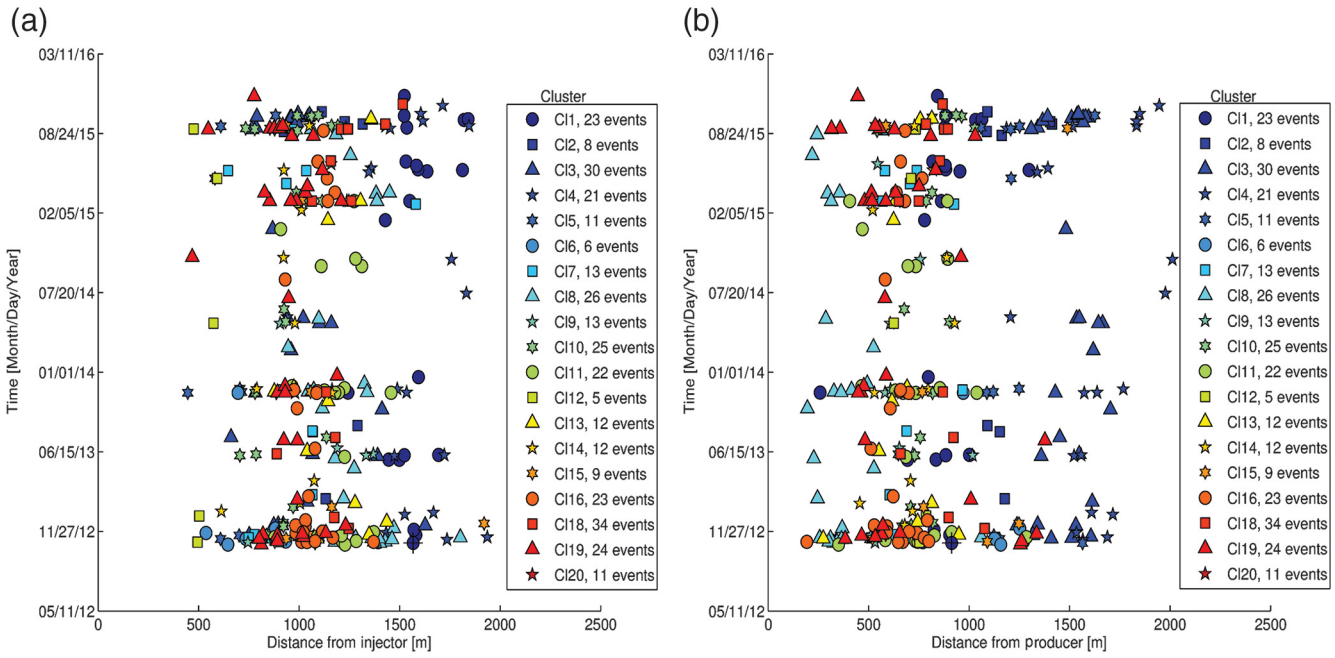

Figure 10. Time–distance plot of induced seismicity at Insheim GPP. (a) Source time versus distance to main flow zone of injection wells. (b) Source time versus distance to main influx of the production well. Symbols indicate members of resolved event clusters with cross-correlation coefficients CC $\geq$ 0.7. The first event recorded after startup of the GPP Insheim is indicated with a black cross. The seismically active volume reached its final size already shortly after startup and remained constant over the hitherto production time.

of cluster 1 shows an oblique normal faulting with north-northeast–south-southwest striking (30.351.12) that might indicate the activation of a crossing fault zone at the beginning of production. Three events of cluster 3 show a steeply dipping normal fault with nearly north–south striking (75.317.12, 77.317.12, and 125.328.12). One event of this cluster shows a steeply dipping northwest–southeast-striking normal faulting and coincides with the northwest-to-southeast-oriented conjugated fault system (74.317.12). Furthermore, three strike-slip events have been observed within cluster 10, 18, and 20, respectively, and likely coincide with the northwest-to-southeast-oriented conjugated fault system (60.269.15, 43.269.15, and 65.272.15). The FPS thus support the complex geometry of the activated fault system revealed by the double-difference relocation.

To evaluate the temporal evolution of the seismically active volume, time–distance plots have been created relative to the main flow zone of the injection well, as well as relative to the main influx zone of the production well (Fig. 10). The figure reveals no classical r–t plot, with r the triggering front and t the time from the injection start, as known from injection experiments or stimulation procedures with one point injectors (e.g., Shapiro and Dinske, 2009). The Insheim reservoir is a hydrothermal system connected to a large fluid reservoir within a highly fractured rock matrix with natural fluid paths. This is different from classical HDR environments (e.g., Soultz-sous-Forêts), and a simple diffusion process describing the migration of the trigger front cannot be assumed. No exponential increase of the time–distance function that could be suitable for estimating diffusivity and thus hydraulic permeability (Shapiro and Dinske, 2009) is visible. The final size of the seismically active volume has been reached shortly after startup of the GPP and remained stable during the production time (see Figs. 5 and 10). From the beginning of operation, a considerable complexity in the spatio-temporal distribution of induced seismicity (no simple systematic migration of the seismicity from the injection wells to the production well) is observed at the GPP Insheim. Individual spatial clusters are activated at different times and sometimes occur as earthquake swarms that have also been found in a previous study by Grund *et al.* (2016). Interestingly, cluster 1 consisting of 23 events, including the first recorded event in the reservoir after startup of the GPP was activated repeatedly, with a larger nonactive time period in 2014. Also cluster 8, which includes the largest events recorded in the Insheim reservoir and which is close to the production well, was activated in 2013, starting with the magnitude 1.9 reference event after the pumping failure, and has been reactivated repeatedly throughout the entire production time.

It is well accepted that fluid-injection seismicity occurs when the pore-fluid pressure on a fault is increased, thus reducing the normal stresses acting on the fault. If the fault is favorably oriented with respect to the pending tectonic stress field, the tectonic forces might lead to shearing of the fault, resulting in a seismic event. At a first glance, it might be contradictory to this model that seismic events are also induced at the production well. At the production well, the pore-fluid pressure is decreased. However, also at the production well], the pressure gradient along faults providing pathways for fluids is large, similar to the injection

well. The fluids flow in the direction of the negative-pressure gradient. Because the fluids have finite shear strength due to a high degree of mineralization, the effective normal stress on the fault can be reduced by the fluids by an amount that is, however, lower than the pressure gradient caused by the production well. If the effective normal stress gets lower than the shear stress acting on the fault, a seismic event is induced.

Conclusions

Long-term observation and accurate location of induced seismicity proved to be the key for understanding the behavior of the geothermal reservoir at Insheim in the central URG. Application of the advanced processing chain HYPOSAT ⇒ VELEST ⇒ NonLinLoc ⇒ hypoDD led to highly accurate hypocenter locations of fluid-injection-induced microearthquakes in the Insheim geothermal reservoir. Using 6810 *P* picks and 6644 *S* picks of 441 well-locatable induced events with magnitudes up to M_L 2.4, we were able to reduce the rms travel-time residual from $rms_{TT} = 1.2$ s to $rms_{TT} = 0.03$ s. We found that velocity models derived from controlled-source methods might be inappropriate for direct use for reliable earthquake location, mainly due to the lack of *S*-wave energy and different source–receiver geometries.

The major part of the seismicity in the Insheim reservoir occurs at depths of ≈4000 m and thus in the crystalline basement, which has also been observed at other fluid-injection operations. Absolute location uncertainties are between 500 and 1000 m in focal depth and between 100 and 300 m in the epicenter, depending on the number of available onset times (see Ⓔ Fig. S6). Relative location errors are in the range of about 50 m. Induced events with highly similar waveforms are within 50–100-m absolute offset giving independent support for the relative location accuracy. The improvement of hypocenter resolution is also shown by the location of the reference event in the immediate vicinity of the production bottom hole that has been recorded by the pressure gauge in the production well and that has formerly been located unrealistically deep below the production well.

Using the high-precision relocations, we were able to clearly resolve six main seismically active regions. Most of the seismicity occurred on an almost north–south-trending fault connecting the injection and production wells. The region between the wells shows several subclusters of events that indicate heterogeneities within this volume with indication for activation of a conjugate fault system. This fault system is crossing the north–south-trending fault in north–northwest to east–eastsouth. They were activated during an early stage of the production of the GPP Insheim and became aseismic after approximately one month of production. Furthermore, one main cluster including the largest events observed in the reservoir and also the reference event is located close to the bottom of the production well (Fig. 5). In total, 20 clusters of highly similar events have been detected. Some occur as earthquake swarms, but often the activity within the clusters spreads over weeks to months, pointing to repeating events.

The spatiotemporal evolution of the seismicity is rather complex. No simple migration of the seismicity has been observed. Briefly, after starting operation, seismicity is located close to both the injection and production wells. Seismic activity is closely related to the injected flow rates and increased repeatedly after shut-ins. Also, at constant flow rates, seismicity scattered in time and space is observed. The estimated seismically active volume reached its final size shortly after startup of GPP Insheim and remained nearly stable throughout the operation time with an estimated volume of $\approx 1.65 \times 10^9$ m^3 (Fig. 10).

FPS calculated from first-motion polarities agree well with observed fault zones derived from active VSP measurements and with the regional stress regime but reflect also the complexity of the reservoir. Three strike-slip events might coincide with the former unknown fault zone oriented from east-eastsouth to north-northwest.

Data and Resources

Seismological data used in this study are partly available at Bundesanstalt für Geowissenschaften und Rohstoffe (BGR) at https://www.bgr.bund.de/EN/Themen/Seismologie/Seismologie/Wellenformdaten/wellenformdaten_node.html (last accessed September 2018) or via ArcLink service at eida.bgr.de:18001. Technical details of the acquisition system Summit VIPA can be found at https://www.summit-system.de (last accessed June 2018). One map was made with QGIS Geographic Information System, Open Source Geospatial Foundation at https://www.qgis.org/de/site/ (last accessed September 2018) and with OpenStreetMap at https://openstreetmap.org (last accessed September 2018). One map was made with Generic Mapping Tools (GMT) at https://www.soest.hawaii.edu/gmt (last accessed May 2018). The magnitude of the natural seismic event close to Herxheim was taken from http://lgrb-bw.de/erdbeben/led_pool/extra_table.htm (last accessed January 2016). The operation data and the seismological data of the permanent stations provided by the operator are not publically available.

Acknowledgments

The authors thank the Federal Ministry for Economy and Energy (Bundesministerium für Wirtschaft und Energie [BMWi]) for funding within the collaborative research project MAGS2 (Wegler *et al.*, 2017, Grant Number MAGS2:0325662A) and the project-executing organization PTJ (Projektträger Jülich) for the support. Furthermore, the authors thank the Federal Agency for Geosciences and Resources (Bundesanstalt für Geowissenschaften und Rohstoffe [BGR]) for managing the project, providing data, and the fruitful collaboration. The authors thank the Pfalzwerke geofuture GmbH for providing the operation data of the geothermal power plant (GPP) Insheim. The authors thank Editor-in-Chief Thomas Pratt, Associate Editor Cezar Trifu, Manuscript Coordinator Betty Schiefelbein, and two anonymous reviewers for their constructive reviews that helped improve the article.

References

Andrews, J., and W. Pettitt (2009). Microseismic monitoring at Landau and Insheim geothermal sites—Processing report October 2007 to September 2009, *Technical Report*, Applied Seismology Consultants.

Applied Seismology Consultants (2014). *InSite User Manual v.3.2. Technical Appendix*, Itasca International Inc.

Baujard, C., A. Genter, V. Maurer, E. Dalmais, J.-J. Graff, and J. Schmittbuhl (2014). The ECOGI EGS project in Rittershoffen, France, *Trans. Geoth. Resour. Counc.* **38,** 267–270.

Baumgärtner, J., and C. Lerch (Editors) (2013). *The Insheim Geothermal Power Plant—The Second Generation of Geothermal Power Plants in the Upper Rhine Graben*, BESTEC GmbH, Mainz, Germany.

Bönnemann, C., B. Schmidt, J. Ritter, N. Gestermann, T. Plenefisch, U. Wegler, R. Schulz, O. Heidbach, K. Erbas, S. Baisch, *et al.* (2010). Das seismische Ereignis bei Landau vom 15 August 2009—Abschlussbericht der Expertengruppe Seismisches Risiko bei hydrothermaler Geothermie, *Technical Report*, Bundesanstalt für Geowissenschaften und Rohstoffe, Hannover, Germany (in German).

Dahm, T., D. Becker, M. Bischoff, S. Cesca, B. Dost, R. S. Fritschen, H. C. Klose, D. Kühn, S. Lasocki, T. Meier, *et al.* (2012). Recommendation for the discrimination of human-related and natural seismicity, *J. Seismol.* **17,** 197–202.

Derer, C., M. Schumacher, and A. Schäfer (2005). The northern upper Rhine graben: Basin geometry and early syn-rift tectono-sedimentary evolution, *Int. J. Earth Sci.* **94,** 640–656.

Diehl, T., T. Kraft, E. Kissling, and S. Wiemer (2017). The induced earthquake sequence related to the St. Gallen deep geothermal project (Switzerland): Fault reactivation and fluid interactions imaged by microseismicity, *J. Geophys. Res.* **122,** no. 9, 7272–7290.

Eulenfeld, T., and U. Wegler (2016). Measurement of intrinsic and scattering attenuation of shear waves in two sedimentary basins and comparison to crystalline sites in Germany, *Geophys. J. Int.* **205,** 744–757.

Evans, K., A. Zappone, T. Kraft, N. Deichmann, and F. Moi (2012). A survey of the induced seismic responses to fluid injection in geothermal and CO_2 reservoirs in Europe, *Geothermics* **41,** 30–54.

Fäh, D., M. Gisler, B. Jaggi, P. Kästli, T. Lutz, V. Masciadri, C. Matt, D. Mayer-Rosa, D. Rippmann, G. Schwarz-Zanetti, *et al.* (2009). The 1356 Basel earthquake: An interdisciplinary revision, *Geophys. J. Int.* **178,** 351–374.

Geiger, L. (1912). Probability method for the determination of earthquake epicenters from the arrival times only (translated from German), *Bull. Seismol. Soc. Am.* **80,** 1605–1628.

Gomberg, J., K. Shedlock, and S. Roecker (1990). The effect of *S*-wave arrival times on the accuracy of the hypocenter estimation, *Bull. Seismol. Soc. Am.* **80,** 1605–1628.

Groos, J., R. Fritschen, and J. Ritter (2013). Untersuchung induzierter Erdbeben hinsichtlich ihrer Spürbarkeit und eventueller Schadenswirkung anhand der DIN 4150, *Bauingenieur* **88,** no. 9, 374–384 (in German).

Grund, M., J. Groos, and J. Ritter (2016). Fault reactivation analysis using microearthquakes clustering based on signal-to-noise weighted waveform similarity, *Pure Appl. Geophys.* **173,** no. 7, 2325–2355.

Hardebeck, J., and P. Shearer (2002). A new method for determining first-motion focal mechanisms, *Bull. Seismol. Soc. Am.* **92,** 2264–2276.

Häring, M., U. Schanz, F. Ladner, and B. Dyer (2008). Characterisation of the Basel 1 enhanced geothermal system, *Geothermics* **37,** 469–495.

Husen, S., and J. Hardebeck (2010). Earthquake location accuracy, *Community Online Resource for Statistical Seismicity Analysis*.

Kinnaert, X., E. Gaucher, U. Achauer, and T. Kohl (2016). Modelling earthquake location errors at a reservoir scale: A case study in the upper Rhine graben, *Geophys. J. Int.* **206,** 861–879.

Kissling, E. (1988). Geotomography with local earthquake data, *Rev. Geophys.* **26,** 659–698.

Kissling, E., W. Ellsworth, and R. Cockerham (1984). Three-dimensional structure of the Long Valley Caldera, California, region by geotomography, *U.S. Geol. Surv. Open-File Rept. 84-939*, 188–220.

Kissling, E., W. Ellswoth, D. Eberhart-Phillips, and U. Kradolfer (1994). Reference models in local earthquake tomography, *J. Geophys. Res.* **99,** 19,635–19,646.

Kölbel, T., P. Schlagermann, W. Münch, D. Rettenmaier, and R. Zorn (2010). *Geothermiekraftwerk Bruchsal: Erste Messergebnisse*, Fachmagazin für Brunnen- und Leitungsbau, 2–7 (in German).

Leydecker, G. (2011). Erdbebenkatalog für Deutschland, *E. Bundesanstalt für Geowissenschaften und Rohstoffe und dem Landesamt für Bergbau, Energie und Geologie*, Vol. 59 (in German).

Lomax, A., J. Virieux, P. Volant, and C. Berge (2000). Probabilistic earthquake location in 3D layered models: Introduction of a Metropolis-Gibbs method and comparison with linear locations, in *Advances in Seismic Event Location*, Kluwer, Amsterdam, The Netherlands, 101–134.

Majer, E., R. Baria, M. Stark, S. Oates, J. Bommer, B. Smith, and H. Asanuma (2007). Induced seismicity associated with enhanced geothermal systems, *Geothermics* **36,** 185–222.

Maxwell, S., and R. Young (1993). A comparison between controlled source and passive source seismic velocity images, *Bull. Seismol. Soc. Am.* **83,** no. 6, 1813–1834.

Megies, T., and J. Wassermann (2014). Microseismicity observed at a non-pressure-stimulated geothermal power plant, *Geothermics* **52,** 36–49.

Mergner, H., L. Eggeling, T. Kölbel, W. Münch, and A. Genter (2012). Geothermische Stromerzeugung: Bruchsal und Soultz-sous-Forêts, *Mining + Geo* **4,** 666–673 (in German).

Michelini, A., and B. Bolt (1986). Application of the principal parameters method to the Coalinga, California, aftershock sequence, *Bull. Seismol. Soc. Am.* **76,** 409–420.

Misiek, R., S. Bißmann, C. Witte, and P. Bergmann (2009). Neubearbeitung 2D reflexionsseismischer Daten im Raum Insheim bei Landau, *Technical Report*, DMT GmbH & Co. KG (in German).

Niitsuma, H., M. Fehler, R. Jones, S. Wilson, J. Albright, A. Green, R. Baria, K. Hayashi, H. Kaieda, K. Tezuka, *et al.* (1999). Current status of seismic and borehole measurements for HDR/HWR development, *Geothermics* **28,** 451–692.

Orywall, P., T. Kölbel, W. Münch, A. Genter, J.-J. Graff, and N. Cuenot (2009). Das EGS-Projekt Soultz-sous-Forêts: Von der Reservoirentwicklung zur Stromproduktion, *Fachmagazin für Brunnen- und Leitungsbau*, 52–59 (in German).

Paige, C., and M. Saunders (1982). LSQR: Sparse linear equations and least squares problems, *ACM Trans. Math. Software* 8**,** no. 2, 195–209.

Peters, G., and R. T. van Balen (2007). Tectonic geomorphology of the northern upper Rhine graben, Germany, *Global Planet. Change* **58,** nos. 1/4, 310–334.

Pribnow, D., and R. Schellschmidt (2000). Thermal tracking of upper crustal fluid flow in the Rhine graben, *Geophys. Res. Lett.* **27,** no. 13, 1957–1960.

Reiter, K., O. Heidbach, J. Reinecker, B. Müller, and T. Röckel (2015). Spannungskarte Deutschland 2015, *Erdöl Erdgas Kohle* **131,** no. 11, 437–442 (in German).

Ritter, J., M. Wagner, and K.-P. Bonjer (2005). The 2005 Heidelberg and Speyer earthquakes and their relationship to active tectonics in the central upper Rhine graben, *Int. J. Earth Sci.* **98,** 697–705.

Schellschmidt, R., and C. Clauser (1996). The thermal regime of the upper Rhine graben and the anomaly at Soultz, *Z. angew. Geol.* **42,** 40–43.

Schumacher, M. (2002). Upper Rhine graben: Role of preexisting structures during rift evolution, *Tectonics* **21,** no. 2, 1–17.

Schweitzer, J. (2001). HYPOSAT—An enhanced routine to locate seismic events, *Pure Appl. Geophys.* **158,** 277–289.

Shapiro, S., and C. Dinske (2009). Fluid-induced seismicity: Pressure diffusion and hydraulic fracturing, *Geophys. Prospect.* **57,** 301–310.

Stange, S. (2006). M_L determination for local and regional events using a sparse network in southwestern Germany, *J. Seismol.* **10,** 247–257.

Tarantola, A., and B. Valette (1982). Inverse problems = Quest for information, *J. Geophys.* **50,** 159–170.

VanWees, J.-D., T. Boxem, L. Angelino, and P. Dumas (2014). A prospective study on the geothermal potential in the EU, *Technical Report*, GEOELEC.

Waldhauser, F. (2001). hypoDD—A program to compute double-difference hypocenter locations, *U.S. Geol. Surv. Open-File Rept. 01-113*.

Waldhauser, F., and F. Ellsworth (2000). A double-difference earthquake location algorithm: Method and application to the northern Hayward fault, *Bull. Seismol. Soc. Am.* **90,** 1353–1368.

Wegler, U., M. Pilger, T. Plenefisch, B. Schmidt, J. Wassermann, W. Friederich, T. Meier, T. Spies, J. Schlittengard, S. Shapiro, *et al.* (2017).

Mikroseismische Aktivität geothermischer Systeme 2—Vom Einzelsystem zur großräumigen Nutzung (Microseismic Activity of Geothermal Systems), *Open-File Report 0325662A-G* (in German).

Zang, A., V. Oye, P. Jousset, N. Deichmann, R. Gritto, A. McGarr, E. Majer, and D. Bruhn (2014). Analysis of induced seismicity in geothermal reservoirs—An overview, *Geothermics* **51,** 6–21.

Ziegler, P. (1992). European Cenozoic rift system, *Tectonophysics* **208,** 91–111.

BESTEC GmbH Landau
Oskar-von-Miller-Straße 2
D-76829 Landau
Germany
kueperkoch@bestec-for-nature.com
(L.K.)

Institute of Geophysics
Christian-Albrechts-University Kiel
D-24118 Kiel
Germany
kai.olbert@ifg.uni-kiel.de
thomas.meier@ifg.uni-kiel.de
(K.O., T.M.)

Manuscript received 8 December 2017;
Published Online 25 September 2018